Acta Crystallographica Section A
Foundations of Crystallography
ISSN 0108-7673

Received 14 January 2009
Accepted 15 July 2009

Using dynamically scattered electrons for three-dimensional potential reconstruction

Christoph T. Koch

Max Planck Institut für Metallforschung, Heisenbergstrasse 3, 70569 Stuttgart, Germany.
Correspondence e-mail: christophtkoch@web.de

Three-dimensional charge-density maps computed by first-principles methods provide information about atom positions and the bonds between them, data which are particularly valuable when trying to understand the properties of point defects, dislocations and interfaces. This paper presents a method by which three-dimensional maps of the electrostatic potential, related to the charge-density map by the Poisson equation, can be obtained experimentally at 1 Å resolution or better, especially at low accelerating voltages. The method requires data acquired by holographic transmission electron microscopy methods such as off-axis electron holography or focal series reconstruction for slightly (*e.g.* $\pm 2^\circ$) different directions of the incident electron beam. The reconstruction of the three-dimensional electrostatic (and absorptive) potential is achieved by making use of changes in the dynamical scattering within the sample as the direction of the incident beam varies.

1. Introduction

Extended defects such as dislocations and interfaces, in particular solid–liquid interfaces, pose a particular challenge to atomic scale computational methods. While their complexity normally requires supercells too large for *ab initio* methods, the long-range nature of forces determining their properties [*e.g.* strain fields, Coulomb and van der Waals (dispersion) forces] makes the construction of reliable yet efficient interatomic potentials, required for molecular dynamics and related computational methods, an extremely complicated task. Being able to perform experiments which directly map the three-dimensional local electrostatic potential would provide a wealth of information. In the case of molecular dynamics simulations, for example, it would allow verification of interatomic potentials by direct comparison between experiment and simulation for the very (defect) structure under investigation. For single crystals of small unit cell it has recently been demonstrated that it is possible to map the bond charge distribution by fitting Fourier coefficients of the crystal potential to convergent beam electron diffraction (CBED) data (Zuo *et al.*, 1999).

Transmission electron microscopy (TEM) images, in the context of focal series reconstruction (inline holography) over a large defocus range (Koch, 2008*b*), are very sensitive to relative atomic positions and variations in the electrostatic potential. Although claiming to be able to provide data on the three-dimensional distribution of atoms, this is not true for destructive methods such as the three-dimensional atom probe (Blavette *et al.*, 1993) because the atoms being 'imaged' are not extracted from their original environment but from the sample surface.

The enormous advantages of TEM imaging come at the price of the lack of a general direct interpretability at atomic resolution. Although modern electron optics has been able to produce more directly interpretable images by removing many of the additional contrast features owing to coherent lens aberrations, in many cases the images are still not directly interpretable because of the multiple (or dynamical) scattering of electrons within the sample itself. This is the main reason why electron tomography has never been applied at atomic resolution, with the exception of extremely small nanostructures consisting of light atoms, for which the authors felt that they could neglect dynamical electron scattering events (Sadan *et al.*, 2008). Also, at very high resolution it becomes generally difficult to keep the sample within the field of view when tilting the sample holder, making automated acquisition a great challenge.

Attempts to correct for such multiple scattering 'artifacts' (*i.e.* features which cannot be interpreted directly in terms of the projected electron density and atom core positions) in the exit face wavefunction have, in the case of thin or non-crystalline samples, at most been able to reconstruct the projected potential, averaged along the direction of the electron beam (Gribelyuk, 1991; Beeching & Spargo, 1993; Scheerschmidt & Knoll, 1994; Scheerschmidt, 1998; Lentzen & Urban, 2000; Allen *et al.*, 2001). Applying such a reconstruction of the projected potential to remove the effect of multiple scattering in tomography assumes that the average potential reconstructed for a given projection represents the potential

everywhere along the direction of projection, an assumption that restricts the application of such methods to homogeneous samples only.

The method presented below reconstructs directly the local complex scattering potential, the real part of which is the electrostatic potential, on a three-dimensional grid by separating the multiple scattering paths between potential voxels.

2. Real-space multislice algorithm

The following discussion will, in order to keep the equations readable, only consider the reconstruction of a two-dimensional structure from a series of one-dimensional images. The extension to three dimensions is straightforward, requiring only small changes in the presented formalism.

The proposed reconstruction method is based on the real-space variant (van Dyck, 1980) of the multislice algorithm (Cowley & Moodie, 1957) for solving the relativistically corrected Schrödinger equation describing the propagation of a fast electron through the specimen potential (see Fig. 1 for an illustration). In a first step the two-dimensional scattering potential (remember that this discussion can easily be extended to three dimensions) is divided into a set of N discrete horizontal slices of thickness ε (the optical axis of the microscope is assumed to be vertical, the fast beam of electrons travelling down the microscope column) and the potential within a slice of index m is projected into a one-dimensional layer of potential

$$V^{(m)}(x) = \int_{\varepsilon(m-1/2)}^{\varepsilon(m+1/2)} V(x, z)\,\mathrm{d}z. \tag{1}$$

The electron propagation is then approximated by multiplication of the incident wavefunction by a phase grating,

$$\Phi^{(m)}(x) = \exp\left[i\sigma V^{(m)}(x)\right], \tag{2}$$

at the position of each slice and Fresnel propagation between the slices, where

$$\sigma = 2\pi\left(m_\mathrm{e}c^2 + E_0\right)/\left[\lambda E_0\left(2m_\mathrm{e}c^2 + E_0\right)\right] \tag{3}$$

is the electron-potential interaction constant (see Fig. 2 for a plot of σ and λ as a function of electron beam energy).

We will assume an incident plane wave $A\exp(2\pi i\mathbf{k}\cdot\mathbf{r}) = A\exp[2\pi i(k_x x + k_z z)]$ arriving at the sample at an angle $\theta = \sin^{-1}(k_x/k_z)$. Since holographic experiments can measure relative phases but not the absolute phase of an electron wavefunction, we will define $z = 0$ in the plane of the exit face wavefunction, fixing the z dependence of the wavefunction at the entrance surface. Including this z-dependent phase factor in the complex but position-independent scaling factor A we obtain $\Psi^{(k_x)}(x) = A^{(k_x)}\exp(2\pi i k_x x)$ at the entrance surface of the specimen. The electron wavefunction at the exit surface can then be obtained by the real-space multislice formalism (van Dyck, 1980) as

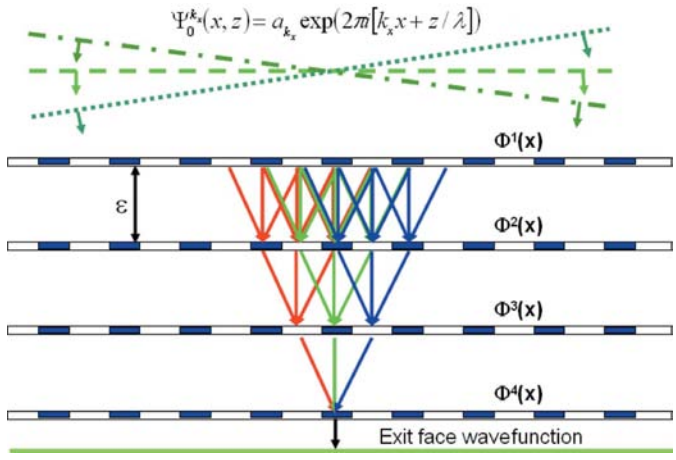

Figure 1
Multislice approximation to dynamical scattering in real space. The scattering of the incident electron beam described by a plane wave is approximated by a finite number of scattering events at equidistant layers partitioning the sample in the z direction. As a consequence, the signal in the exit face wavefunction is non-local, including contributions from a number of scattering paths, the relative phases of which can be varied by changing the illumination tilt angle $\theta_x = \sin^{-1} k_x\lambda$.

$$\begin{aligned}\Psi^{(k_x)}(x) = \Phi^{(N)}(x)\exp\left[\varepsilon\lambda\left(\frac{i\Delta_x}{4\pi} - k_x\nabla_x\right)\right]\cdots \\ \times\,\Phi^{(2)}(x)\exp\left[\varepsilon\lambda\left(\frac{i\Delta_x}{4\pi} - k_x\nabla_x\right)\right]\Phi^{(1)}(x) \\ \times\,A^{(k_x)}\exp(2\pi i k_x x).\end{aligned} \tag{4}$$

Here $\lambda = 1/k_z = hc/[E_0(2m_\mathrm{e} + E_0)]^{1/2}$ is the electron wavelength, E_0 is the accelerating voltage, h is Planck's constant, c is the speed of light, m_e is the mass of an electron, Δ_x is the Laplace operator and ∇_x is the gradient in the x direction.

Implementing the multislice algorithm on a computer requires a discrete grid in the lateral dimension in addition to the discrete slices in the z direction. Keeping the lateral sampling distance δ_x constant, we may simplify the notation by defining a dimensionless imaginary parameter $\gamma_{k_x} = 2\pi i\delta_x k_x$ and replacing x by $j_x\delta_x$, $\Psi(x)$ by Ψ_{j_x}, $V^{(m)}(x)$ by $V_{j_x}^{(m)}$, $\Phi^{(m)}(x)$ by

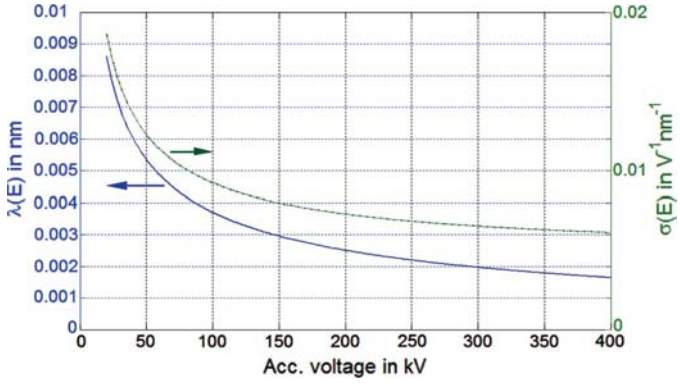

Figure 2
Plot of the electron wavelength λ and electron-potential interaction strength σ as a function of accelerating voltage.

$\Phi_{j_x}^{(m)}$ and $\exp(2\pi i k_x x)$ by $\exp(\gamma_{k_x} j_x)$. This also makes the translation of the following equations into a computer program a bit more apparent.

Expanding the Fresnel propagation operator by using the relations

$$\Delta_x \Psi(x) = \frac{\Psi(x+\delta_x) - 2\Psi(x) + \Psi(x-\delta_x)}{\delta_x^2}, \tag{5}$$

$$\nabla_x \Psi(x) = \frac{\Psi(x+\delta_x) - \Psi(x-\delta_x)}{2\delta_x}, \tag{6}$$

we obtain

$$\begin{aligned}
&\exp\left[\frac{i\varepsilon\lambda}{4\pi}\left(\Delta_x + \gamma_{k_x}\nabla_x\right)\right]\Psi(x) \\
&= \left\{1 + \frac{i\varepsilon\lambda}{4\pi}\left(\Delta_x + \gamma_{k_x}\nabla_x\right) + \frac{1}{2}\left[\frac{i\varepsilon\lambda}{4\pi}\left(\Delta_x + \gamma_{k_x}\nabla_x\right)\right]^2 + \ldots\right\}\Psi(x) \\
&= \Psi(x) + \beta\left[(1+\gamma_{k_x})\Psi_{j_x+1} - 2\Psi_{j_x} + (1-\gamma_{k_x})\Psi_{j_x-1}\right] \\
&\quad + \frac{\beta^2}{2}\left[(1+\gamma_{k_x})^2\Psi_{j_x+2} - 4(1+\gamma_{k_x})\Psi_{j_x+1}\right. \\
&\quad + (6 - 2\gamma_{k_x}^2)\Psi_{j_x} - 4(1-\gamma_{k_x})\Psi_{j_x-1} \\
&\quad \left. + (1-\gamma_{k_x})^2\Psi_{j_x-2}\right] + \mathrm{O}\left(\beta^3\right)
\end{aligned} \tag{7}$$

in orders of approximation of the Ewald sphere curvature given by the parameter

$$\beta = i\varepsilon\lambda/\left(4\pi\delta_x^2\right). \tag{8}$$

The sampling distance δ_x (*i.e.* the detector pixel size divided by the magnification) is typically chosen to be quite a bit smaller than the image resolution defined by aberrations of the electron optics, the stability of the microscope and the size of the objective aperture (*e.g.* 0.1–0.5 Å for high-resolution TEM at 1 Å resolution).

By choosing the appropriate real-space sampling, slice thickness and electron accelerating voltage, one can force β to have a fairly small value. Expression (8) also indicates that for a given real-space sampling δ_x and fixed β the slice thickness ε is inversely proportional to the electron wavelength λ. This means that, in order to achieve convergence in the forward simulation, smaller slice thicknesses must be used at lower accelerating voltages. This also means that for the reconstruction algorithm proposed below a higher resolution in the third dimension may be achieved if the accelerating voltage is decreased.

Plugging the expansion of the Fresnel propagator (7) into (4) we can expand the expression for the exit face wavefunction in orders of β. The first-order expansion neglecting, for the moment, terms of order β^2 and higher is

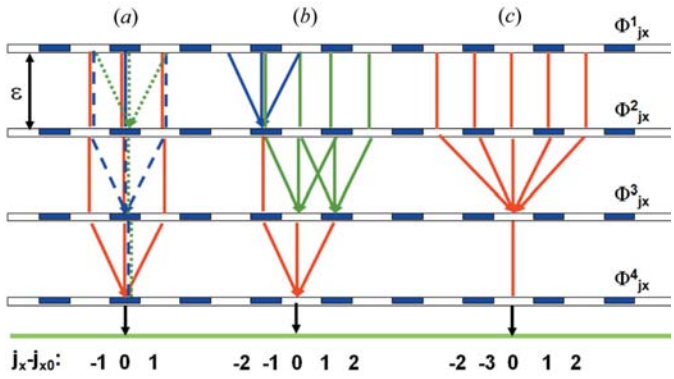

Figure 3
Diagram of the first- (*a*) and second-order (*b*, *c*) approximation of the Ewald sphere curvature effects in the real-space multislice algorithm for $k_x = 0$. The Δ_x operator is depicted by a node merging three paths, and the Δ_x^2 operator by a node merging five paths. Multiplying the scattering potential along the red solid, blue dashed and green dotted paths in (*a*) will produce all the possible terms that are linear in β, *i.e.* which involve only a single Δ_x operator. Terms resulting from paths shown in (*b*) and (*c*) (only one possible path is shown in each) are proportional to β^2 and involve either two successive Δ_x operations or a single Δ_x^2 operation.

$$\begin{aligned}
\Psi_{j_x}^{(k_x)} = A^{(k_x)}\exp\left(\gamma_{k_x} j_x\right)\Phi_{j_x}^{(N)}\left\{\prod_{m=1}^{N-1}\Phi_{j_x}^{(m)}\right. \\
+ \beta\left[\exp\left(\gamma_{k_x}\right)\left(1+\gamma_{k_x}\right)\sum_{k=1}^{N-1}\prod_{m=1}^{k}\Phi_{j_x+1}^{(m)}\prod_{m=k+1}^{N-1}\Phi_{j_x}^{(m)}\right. \\
+ \exp\left(-\gamma_{k_x}\right)\left(1-\gamma_{k_x}\right)\sum_{k=1}^{N-1}\prod_{m=1}^{k}\Phi_{j_x-1}^{(m)}\prod_{m=k+1}^{N-1}\Phi_{j_x}^{(m)} \\
\left.\left. -2(N-1)\prod_{m=1}^{N-1}\Phi_{j_x}^{(m)}\right] + \mathrm{O}(\beta^2)\right\}.
\end{aligned} \tag{9}$$

Note here that the first term, the zeroth-order expansion, is independent of β and is just the well known phase object approximation which includes multiple scattering to the Nth order but neglects effects owing to curvature and tilt of the Ewald sphere.

Fig. 3(*a*) illustrates expression (9) graphically for an object partitioned into four layers. Examples of the two possible scattering paths that scale as β^2 are shown in Figs. 3(*b*) and 3(*c*). While the conventional multislice algorithm (Ishizuka & Uyeda, 1977) iterating between real and reciprocal space naturally includes all orders β^n, in real-space algorithms they need to be included explicitly. Since increasing n slows down the computation enormously, terms $\mathrm{O}(\beta^{n\geq 3})$ in the computation of a single Fresnel propagation are usually neglected. An algorithm approximating the Fresnel propagation up to $\mathrm{O}(\beta^{n=1})$ will only have those contributions of $\mathrm{O}(\beta^{n\geq 2})$ to the final wavefunction of the type shown in Fig. 3(*b*), *i.e.* multiple Δ_x operations, but neglect the equally important contributions shown in Fig. 3(*c*).

3. Solving the inverse problem

The aim of this paper being the determination of the three-dimensional scattering potential from the observed images, we

must consider the contributions to the exit face wavefunction in the order of significance, *i.e.* all terms up to a given order $O(\beta^n)$. Taking a closer look at Fig. 3 makes it clear that in order to reconstruct N slices one needs to expand the Fresnel propagation up to at least $n = (N-1)/2$ (rounding up for even N). The resulting system of polynomial equations of degree N is sparse and may be solved using globally convergent algorithms for solving multivariate polynomial sets of equations [see, for example, Sherali & Tuncbilek (1992) with an example application to the inversion of dynamical CBED patterns given by Koch (2008*a*)]. A more practical method of solving the inverse problem seems to be a refinement approach in which the first initial guess is obtained by the linear approximation (11) to expression (9).

Holographic methods such as off-axis electron holography (Möllenstedt & Düker, 1956; Tonomura *et al.*, 1979; Lichte, 1985), but also focal series reconstruction (Kirkland, 1984; Kirkland *et al.*, 1995; Coene *et al.*, 1996; Kawasaki *et al.*, 2001; Allen & Oxley, 2001; Vincent, 2002; Hsieh *et al.*, 2004; Allen *et al.*, 2004; Bhattacharyya *et al.*, 2006; Koch, 2008*b*), are able to reconstruct the complex exit face wavefunction for each incident beam tilt. If, as is common practice, in the off-axis holographic reconstruction the side band is properly centered, and in the focal series reconstruction the images are aligned by cross-correlation or similar methods, neither of these methods will reconstruct the global phase shift $\exp(\gamma_{k_x} j_x)$ that is associated with the tilted illumination [the relative phase factors in the second and third term of (9) remain though]. We can therefore drop this factor altogether. However, a reference point common to wavefunctions of different incident beam tilt must still be chosen in order to fix the complex coefficients $A^{(k_x)}$. A vacuum region or another area of well known scattering properties within the field of view would be ideal, but if no such reference point can be defined the $A^{(k_x)}$ parameters can also be included as free parameters in the nonlinear reconstruction algorithm. We will assume $A^{(k_x)} = 1$ in the example presented below.

3.1. Linearized reconstruction algorithm

For demonstration purposes, and in order to reveal the principles of the proposed methodology independent of the performance of a given polynomial equation solver, let us approximate the system of polynomial equations (9) by expanding the phase grating $\Phi_{j_x}^{(m)}$ in terms of the potential assuming the validity of the weak phase object approximation. For a structure that has been split into $N = 3$ layers we obtain

$$\begin{aligned}\Phi_{j_{x3}}^{(3)}\Phi_{j_{x2}}^{(2)}\Phi_{j_{x1}}^{(1)} &= \exp\left[i\sigma V_{j_{x3}}^{(3)}\right]\exp\left[i\sigma V_{j_{x2}}^{(2)}\right]\exp\left[i\sigma V_{j_{x1}}^{(1)}\right]\\ &\simeq 1 + i\sigma V_{j_{x3}}^{(3)} + i\sigma V_{j_{x2}}^{(2)} + i\sigma V_{j_{x1}}^{(1)},\end{aligned} \tag{10}$$

converting (9) into the following linear system of equations,

$$\begin{aligned}\Psi_{j_x}^{(k_x)} &\simeq A^{(k_x)}\exp\left(\gamma_{k_x} j_x\right)\Bigg\{1 + i\sigma\sum_{m=1}^{N} V_{j_x}^{(m)}\\ &\quad + \beta\Bigg(\exp\left(\gamma_{k_x}\right)\left(1+\gamma_{k_x}\right)\sum_{k=1}^{N-1}\Bigg\{1 + i\sigma\Bigg[V_{j_x}^{(N)} + \sum_{m=1}^{k} V_{j_x+1}^{(m)}\\ &\quad + \sum_{m=k+1}^{N-1} V_{j_x}^{(m)}\Bigg]\Bigg\}\\ &\quad + \exp\left(-\gamma_{k_x}\right)\left(1-\gamma_{k_x}\right)\sum_{k=1}^{N-1}\Bigg\{1 + i\sigma\Bigg[V_{j_x}^{(N)} + \sum_{m=1}^{k} V_{j_x-1}^{(m)}\\ &\quad + \sum_{m=k+1}^{N-1} V_{j_x}^{(m)}\Bigg]\Bigg\}\\ &\quad - 2(N-1)\Bigg[1 + i\sigma\sum_{m=1}^{N} V_{j_x}^{(m)}\Bigg]\Bigg) + O(\beta^2)\Bigg\}\\ &= A^{(k_x)}\exp\left(\gamma_{k_x} j_x\right)\Bigg(1 + i\sigma\sum_{m=1}^{N} V_{j_x}^{(m)}\\ &\quad + \beta\Bigg\{\exp\left(\gamma_{k_x}\right)\left(1+\gamma_{k_x}\right) i\sigma\sum_{k=1}^{N-1}\Bigg[\sum_{m=1}^{k} V_{j_x+1}^{(m)} + \sum_{m=k+1}^{N-1} V_{j_x}^{(m)}\Bigg]\\ &\quad + \exp\left(-\gamma_{k_x}\right)\left(1-\gamma_{k_x}\right) i\sigma\sum_{k=1}^{N-1}\Bigg[\sum_{m=1}^{k} V_{j_x-1}^{(m)} + \sum_{m=k+1}^{N-1} V_{j_x}^{(m)}\Bigg]\\ &\quad - 2(N-1)\left[1 - \cos(i\gamma_{k_x}) + i\gamma_{k_x}\sin(i\gamma_{k_x})\right]\left[1 + i\sigma V_{j_x}^{(N)}\right]\\ &\quad - 2(N-1) i\sigma\sum_{m=1}^{N-1} V_{j_x}^{(m)}\Bigg\} + O(\beta^2)\Bigg),\end{aligned} \tag{11}$$

the solution of which is almost straightforward. It turns out that the matrix defining the resulting system of equations is slightly rank-deficient, because there remain $N-1$ degrees of freedom, the overall relative phase relationships between the N layers. Defining the relative potential of one column of pixels [*e.g.* in the example shown in Fig. 5 three additional linear equations are defined that force the potential to be zero (vacuum) for the right-most pixel in each of the three layers] will remove this degree of freedom and produce, in the absence of noise, a unique reconstruction. A more general approach, especially if no vacuum is within the reconstructed volume, would be to fix the mean potential of each layer by defining it to be zero. This degree of freedom corresponds to the physically meaningful inability to measure the absolute phase of the electron wavefunction.

The sensitivity with respect to noise of this linearized reconstruction is directly related to the size of the parameters γ_{k_x}, β and σ. If the product $\beta\gamma_{k_x}\sigma$ is zero, the system of equations defined by (11) is rank-deficient and cannot be solved. Fig. 4 shows how the product of these parameters depends on the tilt range and electron beam energy. Although the occurrence of these parameters in (11) is a bit more complicated, to first-order approximation an increase in this product very likely increases the condition number of the resulting system of linear equations and with that the robustness of the reconstruction with respect to noise in the input data. It becomes therefore quite obvious that working at low accelerating voltage will allow the reconstruction to work for very small slice thicknesses ε.

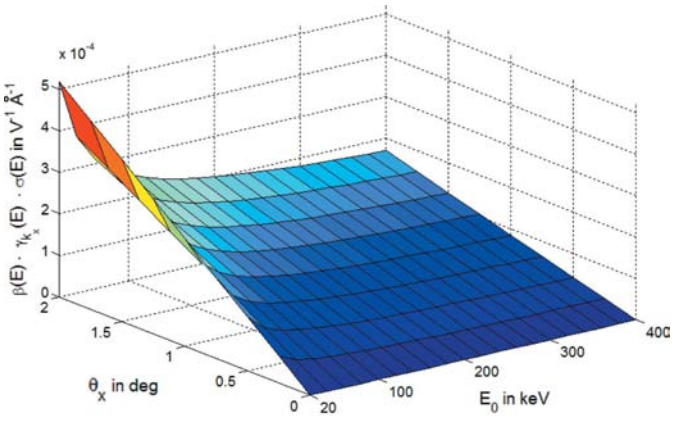

Figure 4
Plot of the tilt-dependent linear independence parameter $\beta\gamma_{k_x}\sigma$ of the system of linear equations (11) as a function of electron beam energy E_0 and tilt angle θ_x for a slice thickness $\varepsilon = 2.04$ Å and sampling $\delta_x = 0.128$ Å. This product is proportional to ε and inversely proportional to δ_x.

3.2. Example

Fig. 5(*a*) shows the phase shift of a trial structure that has been sliced into three equidistant slices. Scattering factors and length scales have been scaled to those of the gold (110) lattice, in order to mimic actual experimental conditions. The system of linear equations (11) has been solved using singular value decomposition, and the result is shown in Fig. 5(*b*). Since no noise has been included in this test, it is not surprising that the reconstruction and original look identical. The fairly low accelerating voltage of only 60 kV causes σ (multiple scattering strength), β (Ewald sphere curvature) and $\beta\gamma_{k_x}$ (illumination tilt sensitivity) to be of large enough values to make a three-dimensional atomic resolution reconstruction of nanostructures feasible, even in the presence of noise and for small beam tilt angles.

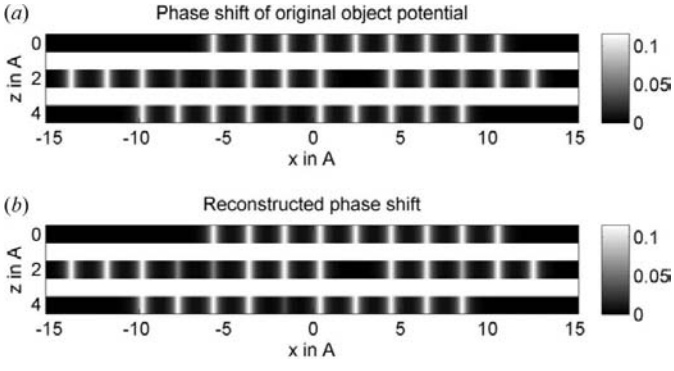

Figure 5
Phase shift $\varphi^{(m)}(x) = \sigma V^{(m)}(x)$ for a three-layered 'phantom' structure (*a*) and the phase shift reconstructed from it using the linear approximation to (9) (*b*) demonstrating a three-dimensional reconstruction at atomic resolution. The scattering factor and lattice constant correspond to that of gold. The 'defect' sites have been created by simply scaling the scattering factor of gold by a number less than 1 (individual defects from left to right; second row: 0.5, 0.5, 0, 0.7; third row: 0.3). Absorption has been included by multiplying the potential $V^{(m)}(x)$ by $(1 + 0.1i)$. Simulation parameters: object potential grid 240 × 3 pixels, $\delta_x = 0.128$ Å, $\varepsilon = 2.04$ Å, $E_0 = 60$ kV, $\sigma = 0.0011$ (V Å)$^{-1}$, $\beta = 0.49i$, five different tilt angles of the incident beam: $\theta = -1^\circ$ ($\gamma_{k_x} = -0.29i$), $\theta = -0.3^\circ$ ($\gamma_{k_x} = -0.086i$), $\theta = 0^\circ$ ($\gamma_{k_x} = 0i$), $\theta = 0.7^\circ$ ($\gamma_{k_x} = 0.20i$), $\theta = 1^\circ$ ($\gamma_{k_x} = 0.29i$).

Some iterative tomographic reconstruction algorithms allow the specimen geometry to be used as a constraint, in principle being able to reconstruct an object consisting of only N distinct layers to be reconstructed from N projections only. The angle between these N projections must, however, be quite large. Although requiring the same minimum number of tilt angles, in contrast to (linear) tomography, where the three-dimensional information is introduced by projecting along different directions, making use of dynamical scattering as proposed here implies a tilt-angle dependent (complex) weighting factor for a set of monomials (individual terms) in the polynomial system of equations (9). These weighting factors depend strongly on the accelerating voltage and can therefore be tuned to the scattering strength of the material, available beam tilt range and desired resolution in the direction parallel to the electron beam. Modern TEMs, being able to achieve atomic resolution imaging at $E_0 \leq 60$ kV (*e.g.* Kisielowski *et al.*, 2008), will therefore be able to image the three-dimensional potential distribution within nanostructures at atomic resolution without having to tilt the specimen.

4. Discussion

4.1. Comparison with linear tomographic reconstruction

The question now arises as to how this reconstruction method compares with conventional linear tomographic reconstruction algorithms. One difference already mentioned is certainly that linear reconstruction algorithms must neglect any multiple scattering effects and will therefore produce artefacts if the input data were produced by dynamically scattered electrons.

Another aspect is the tilt range that is necessary to achieve the desired resolution in the third dimension. Under the assumption of noise-free input data and a perfect (algebraic) tomographic reconstruction algorithm, Fig. 6(*a*) shows the volume in reciprocal space which can be reconstructed for a beam tilt of $\pm 2^\circ$. Note that there is a factor of about ten between the scales of the axes. At a real-space sampling distance of 0.5 Å ($q_x = 1$ Å^{-1}) the achievable resolution in the z direction is at most 1.4 nm, if very many different tilt angles are used. Adding just a little bit of noise to the input data will quickly produce missing-wedge artefacts. This result cannot be altered by changing the accelerating voltage, except for the possible increase or reduction of dynamical scattering effects by lowering or raising the electron beam energy, respectively.

For the same real-space sampling of $\delta_x = 0.128$ Å the Ewald sphere curvature parameter $\beta(E, \delta_x, \varepsilon)$, on the other hand, is still finite for slice thicknesses $\varepsilon = 1$ Å ($q_z = 0.25$ Å^{-1}), which means that, depending on the accelerating voltage and the signal-to-noise ratio of the input data, a very high resolution in the z direction may be achievable.

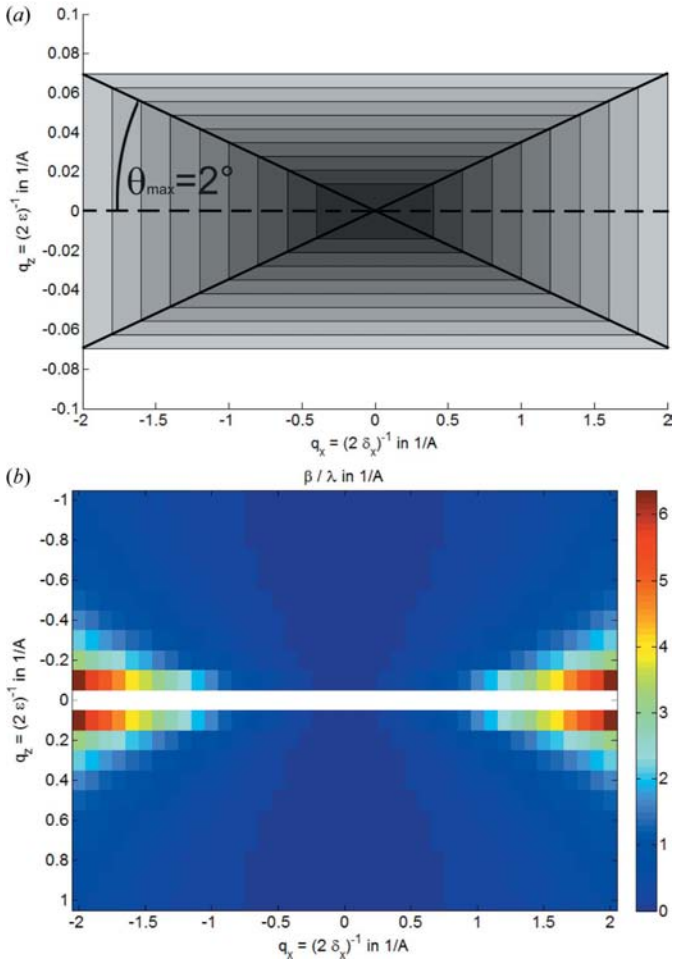

Figure 6
(*a*) Volume in reciprocal space which can be reconstructed from a tilt series spanning a tilt range of -2° to $+2^\circ$. Depending on the real-space sampling along the x direction (δ_x), a corresponding resolution in the z direction of $\varepsilon = \delta_x/\tan(\theta_{\max})$ can be achieved, assuming a perfect reconstruction algorithm and noise-free data. (*b*) The λ-normalized Ewald sphere curvature parameter $\beta(E, \varepsilon, \delta_x)/\lambda$ spans a much larger range of reciprocal space, independent of the tilt range. However, one must look at the combined effects of the parameters β, γ_{k_x} and σ to quantitatively predict the robustness of the reconstruction for a given set of parameters (see also Fig. 4).

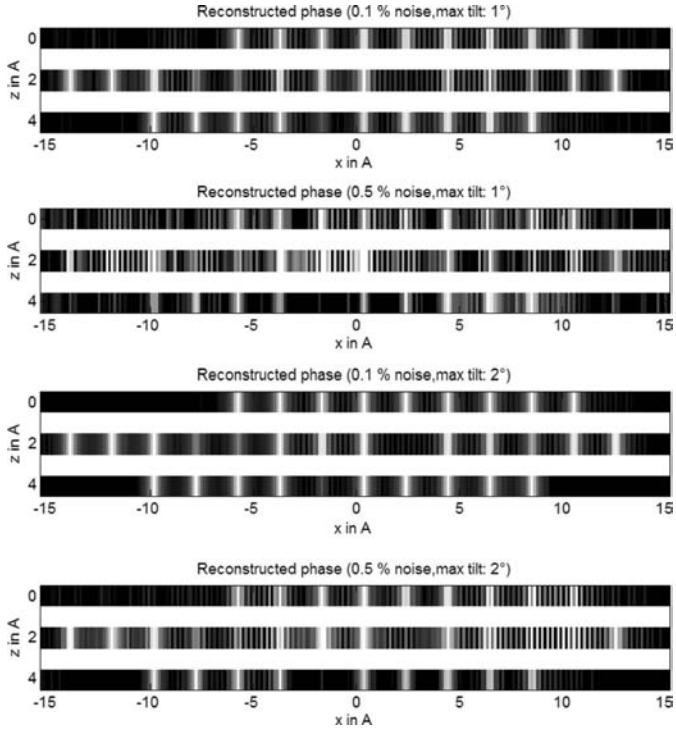

Figure 7
Test of linear reconstruction algorithm for different noise levels and maximum tilt angles. Wavefunctions for seven equally spaced tilt angles (ranging from either -1° to $+1^\circ$ or -2° to $+2^\circ$) were simulated for the object shown in Fig. 5(*a*). Gaussian noise with a standard deviation of 0.1% and 0.5% of the maximum contrast was added independently to the real and imaginary parts of all the wavefunctions. The real part of the three-dimensional reconstructed potential is shown.

4.2. Noise sensitivity

Estimating the effect of noise on the quality of this dynamical scattering inversion scheme would require the simulation of image or hologram intensities, the assumption of proper signal and detector noise statistics, the reconstruction of the individual wavefunctions from either focal series or off-axis holograms, and the three-dimensional reconstruction using this algorithm.

A much more simple, though arguably not the most meaningful, way of doing this is to add Gaussian noise to the complex wavefunctions. Because of being reconstructed from a (large) number of individual images, wavefunctions obtained by focal series reconstruction tend to have very good signal-to-noise properties. Fig. 7 shows reconstructions which have been obtained by adding Gaussian noise to both the real and imaginary parts of the wavefunctions simulated for the complex-valued input object potential used in the example of Fig. 5. The accelerating voltage was again 60 kV, the slice thickness $\varepsilon = 2.04$ Å and the sampling distance $\delta_x = 0.128$ Å. Each of the simulations and subsequent reconstructions was performed for seven equally spaced tilt angles ranging from -1° to $+1^\circ$ for the upper two reconstructions and from -2° to $+2^\circ$ for the lower ones. This result shows how an increase in tilt range can improve the robustness of the reconstruction algorithm.

If this algorithm is used at atomic resolution, additional constraints could be imposed on the reconstructed data. Those constraints could be atomicity (*i.e.* peaks in the potential are assumed to be due to the presence of atoms and cannot therefore be arbitrarily sharp or too close to one another), positivity (both absorption and elastic scattering potential inside the specimen should be positive, and also peaks in the absorption should correlate with peaks in the elastic scattering potential) *etc.* So far, none of these constraints has been imposed, leaving much room for improvement of the robustness of the reconstruction method beyond what has been shown here.

It should also be noted that exit wave reconstruction for several illumination tilt angles is only one of several methods

for acquiring the experimental data required for the three-dimensional reconstruction described above. Alternative methods include Rönchigram focal series recorded for different illumination or specimen shifts and, of course, holographic experiments at different specimen tilts.

5. Conclusion

Summarizing, a method for reconstructing the three-dimensional electrostatic potential of a TEM sample has been proposed. The method is based on a reformulation of a real-space multislice formulation for computing the multiple scattering of a fast electron within a TEM sample in terms of a polynomial set of equations, identifying and keeping the most significant terms. The solution of the resulting sparse multivariate polynomial system of equations can be found by applying either multivariate polynomial equation global optimization algorithms available in the literature or refinement of a solution to the linearized version of the set of equations.

In the special case that the weak phase object approximation is valid, the polynomial system of equations transforms into a linear system of equations which can be solved by standard methods. Applying this simplification, a two-dimensional complex test object consisting of three layers has been reconstructed successfully from five one-dimensional electron wavefunctions simulated for illumination tilt angles ranging from -1° to $+1^\circ$. The construction of an efficient global optimization algorithm specialized for the particular type of systems of polynomial equations described in this paper is planned for the near future.

This work was supported by the European Commission under contract No. NMP3-CT-2005-013862 (INCEMS).

References

Allen, L. J., Koch, C., Oxley, M. P. & Spence, J. C. H. (2001). *Acta Cryst.* A**57**, 473–474.
Allen, L. J., McBride, W., O'Leary, N. L. & Oxley, M. P. (2004). *Ultramicroscopy*, **100**, 91–104.
Allen, L. J. & Oxley, M. P. (2001). *Opt. Commun.* **199**, 65–75.
Beeching, M. & Spargo, A. (1993). *Ultramicroscopy*, **52**, 243–247.
Bhattacharyya, S., Koch, C. T. & Rühle, M. (2006). *Ultramicroscopy*, **106**, 225–238.
Blavette, D., Deconihout, B., Bostel, A., Sarrau, J., Bouet, M. & Menand, A. (1993). *Rev. Sci. Instrum.* **64**, 2911.
Coene, W., Thust, A., Op de Beek, M. & van Dyck, D. (1996). *Ultramicroscopy*, **64**, 109–135.
Cowley, J. M. & Moodie, A. F. (1957). *Acta Cryst.* **10**, 609–619.
Dyck, D. van (1980). *J. Electron.* **119**, 114.
Gribelyuk, M. A. (1991). *Acta Cryst.* A**47**, 715–723.
Hsieh, W.-K., Chen, F.-R., Kai, J.-J. & Kirkland, A. I. (2004). *Ultramicroscopy*, **98**, 99–114.
Ishizuka, K. & Uyeda, N. (1977). *Acta Cryst.* A**33**, 740–749.
Kawasaki, T., Takai, Y., Ikuta, T. & Shimizu, R. (2001). *Ultramicroscopy*, **90**, 47–59.
Kirkland, A. I., Saxton, W. O., Chau, K. L., Tsuno, K. & Kawasaki, M. (1995). *Ultramicroscopy*, **57**, 355–374.
Kirkland, E. J. (1984). *Ultramicroscopy*, **15**, 151–172.
Kisielowski, C. *et al.* (2008). *Microsc. Microanal.* **14**, 469–477.
Koch, C. T. (2008*a*). arXiv:0810.3811v1.
Koch, C. T. (2008*b*). *Ultramicroscopy*, **108**, 141–150.
Lentzen, M. & Urban, K. (2000). *Acta Cryst.* A**56**, 235–247.
Lichte, H. (1985). *Optik*, **70**, 176–177.
Möllenstedt, G. & Düker, H. (1956). *Z. Phys.* **145**, 377–397.
Sadan, M. B., Houben, L., Wolf, S. G., Enyashin, A., Seifert, G., Tenne, R. & Urban, K. (2008). *Nano Lett.* **8**, 891–896.
Scheerschmidt, K. (1998). *J. Microsc.* **190**, 238–248.
Scheerschmidt, K. & Knoll, F. (1994). *Phys. Status Solidi A*, **146**, 491–502.
Sherali, H. D. & Tuncbilek, C. H. (1992). *J. Global Optim.* **2**, 101–112.
Tonomura, A., Matsuda, T., Endo, J., Todokoro, H. & Komoda, T. (1979). *J. Electron.* **28**, 1–11.
Vincent, R. (2002). *Ultramicroscopy*, **90**, 135–151.
Zuo, J., Kim, M., O'Keeffe, M. & Spence, J. (1999). *Nature (London)*, **401**, 49.